M. Alioli, P. Masarati, M. Morandini, T. Carpenter, N.B. Osterberg, R. Albertani
Membrane Shape and Load Reconstruction from Measurements Using Inverse Finite Element Analysis
AIAA Journal, Vol. 55, N. 1, 2017, p. 297-308
doi:10.2514/1.J055123

Membrane Shape and Transverse Load Reconstruction from Measurements Using Inverse Finite Element Analysis

Mattia Alioli[*], Pierangelo Masarati[†], Marco Morandini[†]

Politecnico di Milano, 20156 Milano, Italy

Trenton Carpenter[‡], N. Brent Osterberg[‡], Roberto Albertani[§]

Oregon State University, Corvallis, Oregon, 97330, USA

An original variational formulation is developed for the inverse problem of reconstructing full-field structural displacement and pressure distribution of membrane wings subjected to steady loads from membrane strain distribution. A direct solution approach in co-simulation with fluid-dynamics solvers is also presented. Moving Least Squares are used to smooth and remap surface strain measurements, estimated from digital image correlation, as needed by the inverse solution meshing. The same approach is used to map the structural and fluid interface kinematics and loads during the fluid-structure co-simulation. Both the direct and the inverse analyses are validated by comparing the direct predictions and the reconstructed deformations with experimental data for prestressed rectangular membranes subjected to static and unsteady loads. The load distributions reconstructed using the inverse analysis are compared with the corresponding loads obtained using the direct analysis. The inverse analysis runs on standard off-the-shelf PCs and can be implemented in real-time, providing load distribution estimates at a rate in the order of tens of datasets per second.

[*]Research Assistant, Dipartimento di Scienze e Tecnologie Aerospaziali.
[†]Associate Professor, Dipartimento di Scienze e Tecnologie Aerospaziali.
[‡]Research Assistant, Mechanical Engineering.
[§]Associate Professor, Mechanical Engineering.

submitted

Nomenclature

Symbols

AoA	= Angle of attack	$^\circ$
$\mathbf{D}$	= Plane stress constitutive properties matrix	MPa
$\boldsymbol{\varepsilon}$	= Green-Lagrange membrane strains	
E	= Tensile modulus	MPa
h	= Thickness	mm
ν	= Poisson's modulus	
PS	= Initial prestrain	%
ρ	= Density	kg/m^3
$\boldsymbol{\sigma}$	= Membrane stress tensor	MPa
$\mathbf{T}$	= Pretension's matrix	MPa
$\mathbf{u}$	= Displacement vector	mm
V	= Flow velocity	m/s
w_{ref}	= Reference transverse displacement	mm

Superscripts

(DIC)	= Digital Image Correlation
(fsi)	= Fluid–Structure Interaction analysis
(ifem)	= Inverse Finite Element Model analysis
(m)	= Mapped by MLS

I. Introduction

The work presented within this paper seeks to obtain full-field estimations of the structural displacement and surface stress fields for a membrane wing for Micro Air Vehicle (MAV) applications. The source of these estimations is the elastic wing deformation, experimentally measured in a low-speed wind tunnel using a full-field, non-contact, digital image correlation (DIC) technique, originally developed by researchers at the University of South Carolina [1].

In MAV designs, much like natural fliers, compliant membranes are used to passively enhance flight characteristics [2]. Research on flight utilizing flexible wings within the MAV scale dates back to the 19$^{\text{th}}$ and 20$^{\text{th}}$ century, but only over the last ten to fifteen years, computational fluid dynamic (CFD) simulations and structural finite element models (FEM) have become far more prevalent in this field; this is due to the advent of more powerful, readily available computers. Various numeric fluid-structure interaction simulations were developed for both fixed and flapping wings in order to take into account the coupled behavior of a non-rigid wing and the fluid flow around it [3, 4, 5]. While coupled CFD and FEM models

have proven to be accurate for solving fluid structure interaction problems [3], they are computationally expensive and are not suitable for solving problems in real-time with today's computer technology. In addition to simulation, researchers have also sought to characterize the unsteady flow around flapping (flexible and rigid) wings experimentally [6, 7, 8]. The unsteady fluid structure interactions of membrane wings have been largely investigated, under both steady and dynamic flow conditions [9, 10]. Wings studied were typically rectangular, perimeter reinforced, covered with a thin rubber membrane and had an aspect ratio of two. Membrane wings display unique aerodynamic characteristics due to their aeroelastic nature, which can provide performance improvements over their rigid airfoil counterparts [11]. Extensive research has been conducted on the dynamics of flexible wings, but limited research exists on practical, computationally predictive models dealing with the dynamic behavior of these wings.

A flexible membrane (on a fixed wing) can be successfully treated as inextensible, using a linear stress-stiffening model [12]. The linear stress-strain assumption holds, provided that the strain accumulated due to the aerodynamic load is small in comparison with the prestrain of the membrane.

Because of unsteadiness, flow separation, and turbulence, previous studies using panel methods and simplified laminar solvers have failed to capture the exact effect of membrane wings on performance. To evaluate the effect of aeroelastic cambering on flapping flight performance of flexible wings (at low Reynolds number), an unsteady large-eddy simulation (LES) flow solver was coupled with a linear elastic membrane model with different prestress values [13]. The introduction of camber increases thrust and lift production significantly, although the transverse displacement was up to 25% of the chord, which means a membrane strain of more than 12%. This, in turn, may cause a substantial change of the membrane stress, making the problem strongly nonlinear. In practice, the linearized structural model, which assumes constant membrane prestress, is inadequate for straining of such magnitude.

Currently, the numerical validation of the flow field created by a MAV wing is largely limited to a comparison of numerical aerodynamic coefficients with those garnered through wind tunnel test analysis [14], or to a comparison with flow visualization, focusing on the flow separation, transition, and reattachment locations over the wing [15].

Knowledge of the full-field differential pressure distribution over the wing surface can provide a further level of comparison, indicating areas over the wing where the model may be inadequate. An inverse method could take the deformed wing shapes and estimate the resulting pressure distribution within flight regimes that are difficult, if not impossible to simulate through either CFD or wind tunnel testing.

Aerodynamically, inverse problems have two main applications: they could be used for inverse design problems for optimal airfoil geometries [16], or for structural health monitoring

(an elastic wing is mounted with deformation sensors, typically strain gages or fiber-optics, whose signals are used to reconstruct the displacement field [17], or the original wing loading [18]).

Inverse FEM analysis has been proposed also to identify the mechanical properties of membranes, e.g., when unconventional methods are needed for characterizing the behavior of materials and the associated boundary problems are complex [19, 20]. These methods are applied for example in the identification of the mechanical properties of biological tissues [21].

II. Methodology

A membrane structural model is developed for both direct and inverse dynamics. The direct dynamics analysis is used to predict the deformed shape under specified loads. A membrane finite element, implemented in a multibody formulation [22], is used in co-simulation with a fluid dynamics solver to predict the configuration of the system under static and unsteady loads [23, 24]. The inverse kinematics analysis is used to reconstruct the membrane shape from the membrane strain field. The inverse problem of full-field structural displacement reconstruction is addressed through the application of a variational formulation, leading to a versatile, robust and computationally efficient inverse membrane nonlinear finite element analysis [25], which was inspired by analogous, although linear, approaches developed in the past for shell-like structures [18, 17]. In the current case, nonlinear elasticity is mandatory to capture the essence of the transverse load carrying capability of membranes, whereas in the previously mentioned prior formulations the problem was restricted to linear elasticity: when subjected to a finite amount of transverse displacement, the assumption of constant membrane prestress used in linearized membrane models is no longer acceptable. The complete set of membrane strain measures, consistent with non-linear membrane theory, needs to be used.

Exploiting the functionalities provided by the free software project FEniCS[a] [26] (a collection of libraries specifically designed for the automated and efficient solution of PDEs), a three-node inverse membrane element was developed [27]: three displacement degrees of freedom are used for each node, namely two displacement components in the plane of the membrane and one along the transverse direction. The error function is the difference between the membrane strain measures expressed as functions of the displacements and the corresponding membrane strain measures obtained by re-sampling the experimental strains. A penalty-parameter controlled regularization term mitigates the ill-posedness of the problem, which is associated with the non-uniqueness of the solution in terms of transverse displacement for given membrane stresses and with the high-order nonlinearity of the mem-

[a] http://fenicsproject.org/

brane strains with respect to transverse displacement. In fact, in addition to the usual level of ill-posedness of linear inverse problems (they do not necessarily satisfy conditions of existence, uniqueness, and stability [28, 18]), the present one is also characterized by the fact that for null membrane prestress the elastic problem is exactly singular in configurations that present no transverse displacement of the membrane.

The reconstructed shape of the membrane is used to estimate the surface loads. The actual loads that cause the deformations are unknown; however, their influence is represented in the measured strains. The procedure is verified and validated by correlation with the surface load values predicted by the coupled fluid-structure analysis.

The present work uses an experimental setup that can accurately obtain the full-field three-dimensional displacement and membrane strain over a moderate size wing in wind tunnel testing conditions. Experimental data is based on DIC in conjunction with a load cell and tensile test frame to measure stress and strains: DIC measurements were taken to generate virtual strain sensors on the surface of the membrane [29]. Measurements were further manipulated using moving least-squares (MLS), as illustrated in Ref. [30], to remap the measured displacements and strains on the same grid that is used for the inverse analysis. This form of remapping also produces some amount of spatial filtering.

The proposed methodology enables accurate reconstruction of the three-dimensional displacement field. It may be effectively employed to develop real-time processing of the sensed information. This "inverse" technique (as opposed to conventional "direct" analysis, namely estimating the displacement field from a measured pressure distribution) represents a viable alternative to conventional pressure measurement techniques in low Reynolds number environments. In fact, the thin elastic membrane wing skins used to decrease the vehicle weight and obtain a certain amount of passive shape adaptation [4] are particularly susceptible to intrusive measurements.

Analytical and numerical results, along with experimental measurements of actual membrane wing artifacts subjected to a variety of steady and unsteady flow conditions, are used to validate the proposed formulation.

III. Membrane Inverse Analysis

A membrane is a thin structural element, i.e., an element whose size in one direction (the thickness, z or 3 in the following) is extremely small compared with the other two (x and y or 1 and 2 in the following), see Fig. 1. The transverse gradients of strain and stress components along the reference surface of the membrane are negligible. As a consequence, a membrane cannot withstand transverse loads unless some in-plane prestress is present.

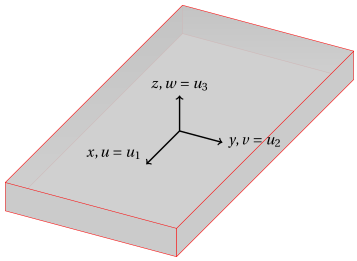

Figure 1. Membrane model.

A. Kinematics

Assuming that in-plane strains are uniform throughout the thickness of the membrane, strain measurements on just one side of the membrane would be sufficient to characterize the in-plane strain field (on the contrary, in the case of a shell, the average of the measurements on both surfaces would be needed to eliminate the effect of bending).

The membrane strains, i.e., the in-plane components of the Green-Lagrange strain tensor, defined as:

$$\varepsilon_x = u_{/x} + \frac{1}{2}\left(u_{/x}^2 + v_{/x}^2 + w_{/x}^2\right) \tag{1a}$$

$$\varepsilon_y = v_{/y} + \frac{1}{2}\left(u_{/y}^2 + v_{/y}^2 + w_{/y}^2\right) \tag{1b}$$

$$\gamma_{xy} = u_{/y} + v_{/x} + u_{/x}u_{/y} + v_{/x}v_{/y} + w_{/x}w_{/y}, \tag{1c}$$

can be collected in a vector $\boldsymbol{\varepsilon}$:

$$\boldsymbol{\varepsilon} = \left\{ \begin{array}{c} \varepsilon_x \\ \varepsilon_y \\ \gamma_{xy} \end{array} \right\} = \left\{ \begin{array}{c} \varepsilon_{11} \\ \varepsilon_{22} \\ 2\varepsilon_{12} \end{array} \right\} \tag{2}$$

or

$$\varepsilon_{ij} = \frac{1}{2}\left(u_{i/j} + u_{j/i} + \mathbf{u}_{/i}^T \mathbf{u}_{/j}\right) \tag{3}$$

where $(\clubsuit)_{/(\spadesuit)}$ indicates the derivative of $(\clubsuit)$ with respect to $(\spadesuit)$, vector $\mathbf{u} = \{u; v; w\} = \{u_1; u_2; u_3\}$ collects the displacement components $u = u_1$ and $v = u_2$ in the plane of the membrane and $w = u_3$ along the transverse direction.

B. Cost Function

The inverse kinematics problem can be formulated by defining an appropriate cost function of the error $\mathbf{e}$ between the measured and the configuration-dependent strains. For this purpose, consider a set of strain measurements $\varepsilon_x^{(\mathrm{m})}$, $\varepsilon_y^{(\mathrm{m})}$, and $\gamma_{xy}^{(\mathrm{m})}$, obtained for example from DIC, namely:

$$\boldsymbol{\varepsilon}^{(\mathrm{m})} = \left\{ \begin{array}{c} \varepsilon_x^{(\mathrm{m})} \\ \varepsilon_y^{(\mathrm{m})} \\ \gamma_{xy}^{(\mathrm{m})} \end{array} \right\}, \tag{4}$$

that correspond to the configuration-dependent strains defined earlier. The error $\mathbf{e}$ is

$$\mathbf{e} = \boldsymbol{\varepsilon}(\mathrm{Grad}(\mathbf{u})) - \boldsymbol{\varepsilon}^{(\mathrm{m})}, \tag{5}$$

with $\mathrm{Grad}(\clubsuit) = \{(\clubsuit)_{/x}; (\clubsuit)_{/y}\}$. The following cost function is considered:

$$\Phi(\mathbf{u}) = \Phi_{\mathbf{e}}(\mathbf{u}) + k\Phi_{\mathbf{u}} \tag{6}$$

where:

- $\Phi_{\mathbf{e}}(\mathbf{u})$ is a quadratic function of the error $\mathbf{e}$,

$$\Phi_{\mathbf{e}}(\mathrm{Grad}(\mathbf{u})) = \frac{1}{2}\int_A \mathbf{e}^T\mathbf{D}\mathbf{e}\ \mathrm{d}A \tag{7}$$

  with $\mathbf{D}$ an arbitrary symmetric, positive definite weighting matrix; e.g., but not necessarily, the plane stress constitutive properties matrix, which for isotropic materials is

$$\mathbf{D} = \frac{E}{1-\nu^2}\left[\begin{array}{ccc} 1 & \nu & 0 \\ \nu & 1 & 0 \\ 0 & 0 & (1-\nu)/2 \end{array} \right] \tag{8}$$

- $\Phi_{\mathbf{u}}$ is a regularization contribution in the derivatives of w,

$$\Phi_{\mathbf{u}}(\mathbf{u}) = \frac{1}{2}\int_A (\mathrm{Grad}(w) - \mathrm{Grad}(w_{\mathrm{ref}}))^T\mathbf{T}(\mathrm{Grad}(w) - \mathrm{Grad}(w_{\mathrm{ref}}))\ \mathrm{d}A \tag{9}$$

  with w_{ref} a reference transverse displacement, defined in the following, and the weight-

ing matrix

$$\mathbf{T} = \begin{bmatrix} T_x & T_{xy} \\ T_{xy} & T_y \end{bmatrix} \tag{10}$$

defined in analogy with the strain energy contribution associated with pre-tension: $T_x > 0$, $T_y > 0$, and $\sqrt{T_x T_y} > |T_{xy}| \geq 0$ such that $\mathbf{T} > 0$ (positive definite);

- k is a parameter that restores dimensional consistency and weighs the regularization contribution.

C. Regularization

The regularization contribution is defined in such a manner that it naturally vanishes at convergence by properly crafting the reference displacement, w_{ref}. Such correction is needed to add a positive definite quadratic contribution to the cost function, and thus make it convex on the entire domain. In fact, the minimization of $\Phi_{\mathbf{e}}(\mathbf{u})$ with respect to the actual displacement field $\mathbf{u}$ requires its partial derivatives with respect to each of the components u, v, and w to vanish. Clearly, as a consequence of the strain definitions of Eq. 1, $\Phi_{\mathbf{e}}(\text{Grad}(\mathbf{u}))$ is not a convex function of w when $\text{Grad}(w) \equiv \mathbf{0}$, i.e., when the membrane is parallel to the reference plane, and the problem is ill-posed in the vicinity of such condition. This approach resembles the so-called damped least squares, also known as the Levenberg-Marquardt algorithm [31, 32].

The inverse formulation does not need elastic or inertial material properties. The reference transverse displacement $w_{\text{ref}} \neq 0$ is needed to deflect the solution towards a specific direction, since the same membrane strain pattern is obtained with $\pm w$. One should choose a tentative initial value for w_{ref}: a convenient choice can be the one corresponding to a uniform pressure difference applied on the membrane, or in any case a prescribed displacement that qualitatively resembles the expected solution [27]. Subsequently, the reference solution is updated by interpolating between the current value $w_{\text{ref}}^{(i)}$ and the solution at the current step i, i.e., $w^{(i)} + \Delta w^{(i)}$, such that at convergence, when $\Delta w^{(i)} \cong 0$, then $(\text{Grad}(w) - \text{Grad}(w_{\text{ref}})) \cong 0$. Thus, $w_{\text{ref}}^{(i+1)} = (1-\alpha) w_{\text{ref}}^{(i)} + \alpha(w^{(i)} + \Delta w^{(i)})$, where $0 < \alpha \leq 1$ is a relaxation parameter ($\alpha = 1$ implies no relaxation).

D. Pressure Field Reconstruction

The estimated displacement field $\mathbf{u} = \{u; v; w\} = \{u_1; u_2; u_3\}$ can be used to estimate the distributed force field $\mathbf{p}$ acting on the membrane [33]:

$$\int_A \delta\boldsymbol{\varepsilon} : \boldsymbol{\sigma} \, \mathrm{d}A = \int_A \mathbf{p} \cdot \delta\mathbf{v} \, \mathrm{d}A \tag{11}$$

where $\boldsymbol{\sigma} = \boldsymbol{\sigma}(\boldsymbol{\varepsilon})$ is the known stress tensor, expressed as a function of the reconstructed strain tensor $\boldsymbol{\varepsilon} = \boldsymbol{\varepsilon}(\mathbf{u})$, and $\delta\mathbf{v}$ is an appropriate vector *test function*, which is required to vanish on the boundary ∂A of A. Thus, the reconstructed distributed force field $\mathbf{p}$ is expected not to be accurate along the boundary of the membrane domain due to the choice of the boundary conditions.

E. Verification

Consider a direct (forward) problem of an edge-clamped square membrane (without pre-strain) bent under the action of the distributed transverse loading (hydrostatic pressure). The strains, computed from the direct problem, are re-sampled to provide the membrane strain values at the points required by the inverse analysis [27, 25]. The re-sampled transverse displacements are used to verify the quality of the inverse analysis. The numerical solution, obtained using a fine mesh (20×20 pairs of elements), has been re-sampled using a much coarser mesh (10×10). A third, intermediate mesh (12×12) has been used for the IFEM procedure.

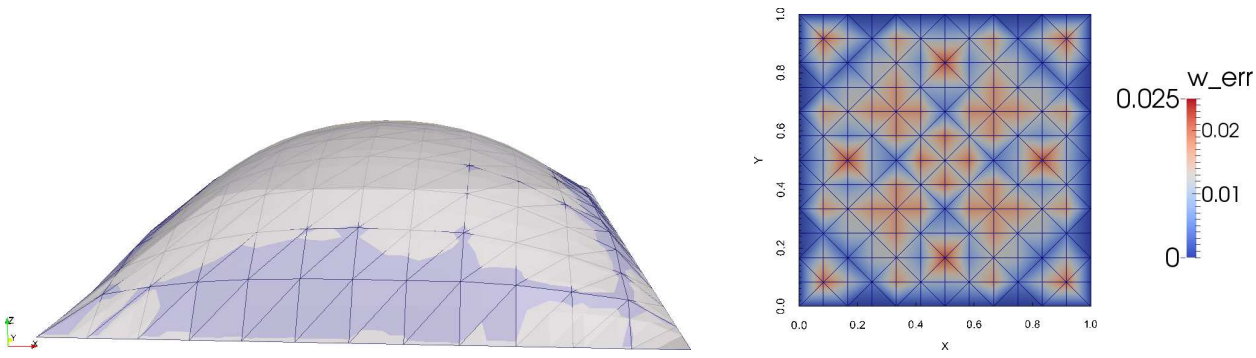

(a) Deformed shape (b) Transverse displacement error

Figure 2. Deformed shape and deformation error of a square membrane subjected to uniform pressure (surface: reference FEM solution; wireframe: IFEM).

Figure 2(a) compares the deformed shape obtained by finite element analysis, with the corresponding deformed shape obtained using the proposed IFEM procedure. Figure 2(b) shows the transverse displacement error, computed as $w_{\mathrm{err}} = |w^{(\mathrm{fem})} - w| / \max|w^{(\mathrm{fem})}|$,

where $w^{(\mathrm{fem})}$ is the transverse displacement obtained by the reference finite element analysis, whereas w is the transverse displacement reconstructed via IFEM.

The estimated displacement field is subsequently used to estimate the pressure acting on the membrane; Table 1 compares the resultant (normal) force error obtained by using the FEM pressure distribution (which is calculated from the displacements of the reference FEM analysis) and the one obtained by using the pressure distribution computed from the displacements estimated via IFEM analysis, with respect to the resultant (normal) force obtained considering the ideal uniform pressure distribution, i.e., pressure times the membrane surface area. To compute the resultant forces, the near-boundary region was omitted from calculation, for the motivation mentioned above.

Table 1. Resultant normal force error (not considering the near-boundary region), comparison of FEM and IFEM analysis with respect to the nominal value.

Reference FEM solution	1.64 %
Inverse FEM analysis	5.25 %

The results, in terms of transverse displacement, are satisfactory. Furthermore, the IFEM and the FEM pressure distributions are quite similar on the entire domain, although both of them are not significantly flat [33]. This is expected, due to the choice of the boundary conditions. Nevertheless, the average values of the pressure distributions calculated using the reconstructed displacements and those from the FEM analysis do seem to be accurate, as shown by the resultant force errors (Tab. 1).

A typical inverse solution like the ones presented above, e.g., with a 12×12 mesh and a residual norm tolerance of 10^{-5}, requires 5 to 8 iterations for each load step. Each iteration requires about 27.5 ms on an off-the-shelf PC (in the present case, an Intel Core i7-2620M with CPU at 2.70 GHz). The property of computational efficiency is of utmost importance since the long term objective is the real-time implementation of the procedure.

F. Problem Well-Posedness

As we shall see, the membrane inverse problem may be ill-posed, and can have multiple solutions. The geometry of a two-dimensional surface is characterized by two symmetric tensors, called the first and second fundamental forms of a surface [34].
Let $\mathbf{x}(\xi^\alpha)$, with $\alpha = \{1,\ 2\}$, be the parametric equations of the surface. Let also $\mathbf{g}_\alpha = \mathbf{x}_{,\alpha} = \frac{\partial \mathbf{x}}{\partial \xi^\alpha}$ and $\mathbf{g}^\alpha$ be the covariant and contravariant surface base vectors, respectively, defined in such a way that $\mathbf{g}_\alpha \cdot \mathbf{g}^\beta = \delta_\alpha^\beta$, the Kronecker delta, with $\alpha,\ \beta = \{1,\ 2\}$.

The first fundamental form $\mathbf{a}$ of the surface is nothing but its metric tensor, defined in such a way that $\mathbf{x}_{,\alpha} = \mathbf{a} \cdot \mathbf{g}_\alpha$. It can be computed as $\mathbf{a} = \mathbf{g}^\alpha \otimes \mathbf{g}_\alpha \cdot \mathbf{g}_\beta \otimes \mathbf{g}^\beta$. The second fundamental form $\mathbf{b}$ of the surface describes the rate of change of the surface normal $\mathbf{n}$,

namely $\mathbf{n}_{,\alpha} = -\mathbf{b} \cdot \mathbf{g}_\alpha$.

The fundamental theorem of the theory of surfaces states that the first and second fundamental forms of a surface determine its shape up to its position in space [35]. In particular, the fundamental theorem of surface theory asserts that, if a field of positive definite symmetric matrices of order two and a field of symmetric matrices of order two together satisfy the Gauss and Codazzi-Mainardi equations (12) in a connected and simply connected open subset of $\mathbb{R}^2$, then there exists a surface in $\mathbb{R}^3$ with these fields as its first and second fundamental forms (global existence theorem) and this surface is unique up to isometries in $\mathbb{R}^3$ (rigidity theorem). Thus, this theorem guarantees that, by knowing both the first and the second fundamental form, the inverse problem of reconstructing the surface is well-posed.

The ill-posedness of the inverse problem comes from the fact that by measuring only the membranal strain tensor $\boldsymbol{\varepsilon}$ one actually accounts only for the first fundamental form, and not for the second. As a matter of fact, the membrane strain tensor $\boldsymbol{\varepsilon}$, Eq. (2), is nothing but the difference between the metric tensor $\mathbf{a}'$ in the deformed configuration $\mathbf{x}' = \mathbf{x} + \mathbf{u}$, computed with respect to the reference configuration, and the metric tensor in the reference configuration $\mathbf{a}$, i.e. $\boldsymbol{\varepsilon} = \frac{1}{2}(\mathbf{a}' - \mathbf{a})$. The difference between the second fundamental form in deformed and reference configuration, i.e., $\mathbf{k} = \mathbf{b}' - \mathbf{b}$, is, instead, a suitable measure of the flexure strain of a thin shell. This means that the inverse problem would be well-posed for a shell model, provided both the membrane and flexure strain are measured.

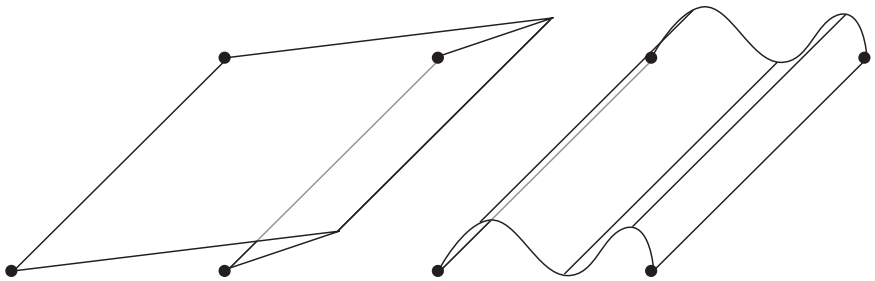

Figure 3. Two possible solutions for a cylindrical bending inverse problem.

As an example of an inverse problem that is not solvable, consider a rectangular membrane made of isotropic material, with Poisson coefficient $\nu = 0$, and subjected to a cylindrical bending with a constant deformation $\varepsilon_{11} = \text{const}$ and all the other deformation components equal to zero, i.e. $\varepsilon_{22} = \varepsilon_{12} = 0$. It is trivial to verify that this problem has not a unique solution. For example, both the deformed configurations of Fig. 3 are among the possible solutions of this problem.

At this point it could be asked whether the inverse procedure described in this report leads to meaningful results, if any. And, indeed, the procedure fails, as it should, when applied to the ill-posed cylindrical bending problem described above. Nonetheless, it appears to work

reasonably well for the test cases that were defined for this activity.

An insight into this apparent paradox comes from the fact that the covariant base vectors $\mathbf{g}_\alpha$ can be used to compute the surface normal as $\mathbf{n} = \frac{\mathbf{g}_1 \times \mathbf{g}_2}{||\mathbf{g}_1 \times \mathbf{g}_2||}$. Then, since $\mathbf{g}_{\alpha,\beta\gamma} = \mathbf{g}_{\alpha,\gamma\beta}$, there must be some compatibility equations between the first and the second fundamental forms. These equations, known as Codazzi-Gauss equations, can be written in many ways. One of them, reported below, is

$$b_{11|2} - b_{12|1} = 0 \tag{12a}$$

$$b_{21|2} - b_{22|1} = 0 \tag{12b}$$

$$b_{11}b_{22} - (b_{12})^2 = Ka \tag{12c}$$

where K is the Gaussian curvature of the surface and $a = \det(\mathbf{a})$. Thus, what makes some problems solvable is the fact that the deformed configuration has a non-null Gaussian curvature, $K \neq 0$, so that a link can be implicitly established between the first and the second fundamental form of the surface.

From a physical point of view, what is really important is that the deformed configuration should not allow an additional bending deformation of the surface that does not involve an additional membrane deformation as well. In other words, the problem should be membrane-dominated [36].

IV. Direct Analysis

The direct analysis is performed using a tightly coupled fluid-structure co-simulation in which the structural problem is solved using the free general-purpose multibody dynamics solver MBDyn[b] [37], developed at Politecnico di Milano, and the fluid problem is solved using a dedicated solver based on FEniCS [23, 24], where systems of Partial Differential Equations (PDE) and corresponding discretization and iteration strategies can be defined in terms of a few high-level Python statements which inherit the mathematical structure of the problem, and from which low level code is automatically generated. The fluid dynamics code is based on a stabilized finite element approximation of the unsteady Navier-Stokes equations (often referred to in the literature as G2 method [38]).

The multibody solver is coupled with the external fluid dynamics code by means of a general-purpose, meshless boundary interfacing approach based on Moving Least Squares with Radial Basis Function [30]. This technique allows to compute a sufficiently regular and accurate approximation of the field of the structural displacements and velocities at the aerodynamic interface nodes, based on a set of structural nodes that is in general irregularly

[b] http://www.mbdyn.org/.

distributed in the neighborhood of the interface. A "fish-bone" structure is obtained by defining two points rigidly offset from each structural node along the normal to the membrane reference plane in opposite directions, to obtain a symmetric layout. This guarantees that node rotations related to bending are correctly transmitted to the aerodynamic wet surface (i.e., the interface matrix is computed using displacements only, without directly involving rotations).

The membrane element implemented in MBDyn is formulated as a four-node isoparametric element based on second Piola-Kirchhoff type membranal resultants [22]. The classical Enhanced Assumed Strains (EAS) method [39] is exploited to improve the response of the element: seven additional variables for each membrane element are added to the strain vector [40].

The stress tensor, reorganized in the form of a vector, can be expressed as a function of the strain tensor, reorganized in the same manner, using the constitutive law of the membrane element given in Eq. (8):

$$\left\{ \begin{array}{c} \sigma_{11} \\ \sigma_{22} \\ \sigma_{12} \end{array} \right\} = \mathbf{D} \left\{ \begin{array}{c} \varepsilon_{11} \\ \varepsilon_{22} \\ \varepsilon_{12} \end{array} \right\}. \tag{13}$$

In case of homogeneous constitutive properties, the forces per unit span are readily obtained by multiplying the stresses by the thickness h of the membrane; otherwise, thickness-wise integration is required. Generically anisotropic constitutive properties can be defined, provided matrix $\mathbf{D}$ is symmetric and positive definite but otherwise arbitrarily set by the user.

V. Results

Since the methods described above are being evaluated for their capability of estimating an actual pressure distribution, it is first necessary to know what the applied pressure is, in order to have a basis for comparison. For this reason, two experiments were conducted in this work to provide different loading scenarios, in order to compare the direct prediction and the reconstructed deformed shape with experimental data for prestressed rectangular membrane wings subjected to hydrostatic pressure loads (Section B) and in steady level flight (Section C).

Correlation is sought with respect to experimental results obtained in test campaigns performed at Oregon State University, where elastic deformations and strains were measured using DIC [29].

Figure 4 summarizes the verification procedure: the strain measurements are first re-

sampled onto the numerical grid that is subsequently used for IFEM analysis by means of a MLS procedure using radial basis functions, discussed in Section A, and initially developed for field interpolation at the interface between fluid and structure [30]. The re-sampled measurements are used as inputs for the IFEM analysis. The re-sampled (transverse) displacements are used to evaluate the quality of the reconstructed displacements via IFEM and those predicted using the tightly coupled fluid-structure co-simulation.

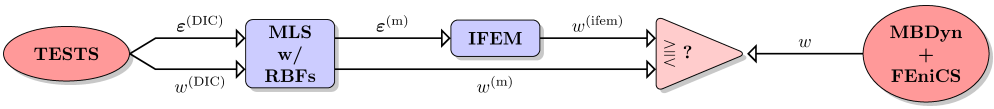

Figure 4. Scheme of the verification procedure.

Furthermore, total force measurements are used to evaluate the total force reconstructed by direct analysis and IFEM, and pressure distributions determined by direct analysis are used to evaluate the pressure distribution reconstructed by IFEM.

A. Experimental Data Re-Sampling

Measurements provided by DIC [29] include the reference location in space of an arbitrary set of points on the surface, arbitrarily chosen by the DIC algorithm when the measurement system is activated, the displacements of the corresponding points in the current sample, and an estimate of the surface strains. Data preparation, for both the measured strains used as inputs and the measured displacements used for correlation, requires re-sampling of unstructured measured fields onto the grid that is subsequently used for IFEM analysis. This is done to reduce the size of the IFEM problem, to avoid distortions in the mesh of the IFEM model, and to obtain an initial spatial filtering of the measurements. For this purpose, a meshless mapping procedure originally developed for fluid-structure coupling is used [30]. The mapping produces a linear interpolation operator, $\mathcal{H}$, from the measurement domain, $(\cdot)_m$, to the virtual sensing domain, $(\cdot)_v$, namely $\mathbf{x}_v = \mathcal{H} \cdot \mathbf{x}_m$.

Operator $\mathcal{H}$ is computed based on the initial positions of the points of both domains; from that point on, it is used to map an arbitrary configuration of the measure domain onto the virtual sensing domain. The participation of each component of a measure point's position to the mapping of the corresponding component of a virtual point is the same, i.e., the mapping is isotropic. As a consequence, any scalar field, as well as each component of any vector field, can be mapped separately using a subset of matrix $\mathcal{H}$, obtained for example by extracting every one out of three columns and rows of matrix $\mathcal{H}$, $\overline{\mathcal{H}} = \mathcal{H}(1{:}3{:}\mathrm{end}, 1{:}3{:}\mathrm{end})$. The component-by-component re-sampled strain measurements, $\boldsymbol{\varepsilon}_{i_v} = \overline{\mathcal{H}}\boldsymbol{\varepsilon}_{i_m}$, $i = 11, 22, 12$,

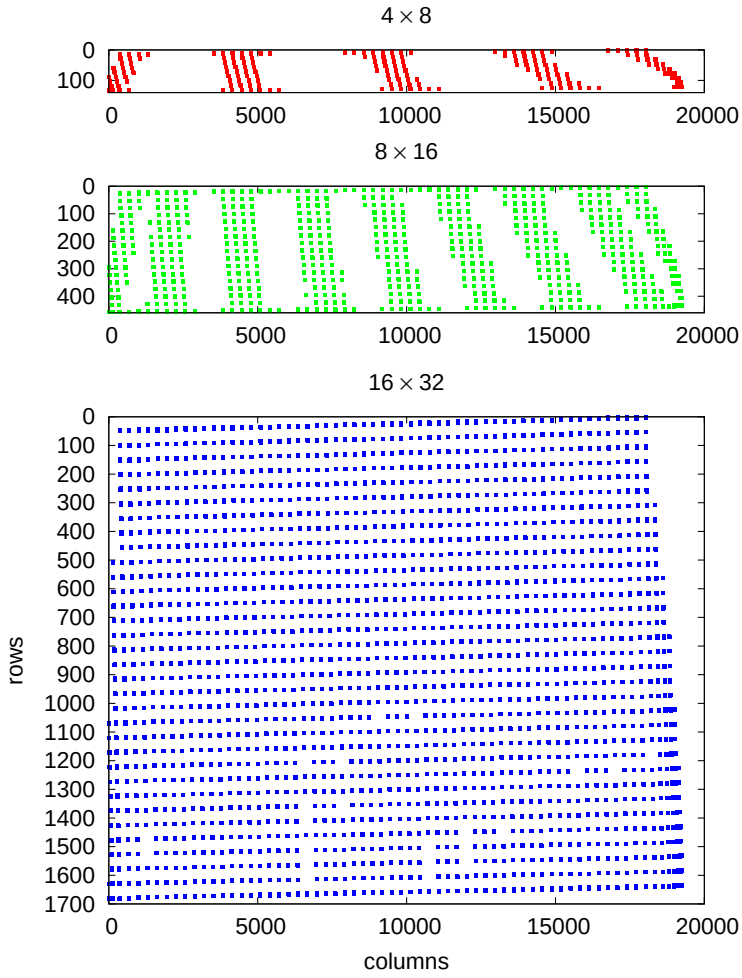

Figure 5. Shape and fill-in of mapping operator $\mathcal{H}$.

are used as inputs for the IFEM procedure, whereas the re-sampled displacements, $\mathbf{u}_v = \mathcal{H}\mathbf{u}_m$, are used to evaluate the quality of the reconstructed displacements.

When a sufficiently large number of measurement points is required to interpolate the position of a virtual sensing point, as occurs in the present case, the procedure also produces a smoothing of the input data, acting as a spatial filter.

Thanks to the compact support used for the interpolation [30], the mapping matrix $\mathcal{H}$ is usually quite sparse: Fig. 5 shows the shape and fill-in (of the order of 0.05 % of non-zeroes) for the 4×8 (45 nodes), 8×16 (153 nodes) and 16×32 (561 nodes) membrane meshes mapped from 6416 DIC points. Since matrix $\mathcal{H}$ is essentially involved only in matrix-vector multiplications, it can be (and is, indeed) stored and handled exploiting such sparsity, thus drastically reducing the computational cost associated with field mapping [27].

B. Hydrostatic Pressure Test

The first scenario was a hydrostatic pressure case, where a pre-tensioned membrane was subjected to a constant, known pressure on one side. DIC measurements of strain and deformation were taken of the deformed membrane.

The experiments [29] refer to a rectangular edge-clamped membrane wing, whose dimensions are $140 \times 75 \times 0.14$ mm. The wing was constructed of a pre-tensioned rubber latex membrane. The material properties are reported in Table 2. The membrane, prestrained by a 9% isotropic membrane strain ($\varepsilon_{x_0} = \varepsilon_{y_0} = 0.09$, $\gamma_{xy_0} = 0$), was subjected to hydrostatic pressure differences between the lower and the upper surface ranging from 100 Pa to 500 Pa in steps of 100 Pa.

Table 2. Membrane material properties.

	Tensile modulus E	Poisson's modulus ν	Density ρ
latex rubber	1.6 MPa	0.4	1350. kg/m^3
steel frame	210 GPa	0.3	7800. kg/m^3

1. *Direct Survey*

Figures 6(a) and 6(b) compare the numerical results for the problem with 300 Pa and 500 Pa of pressure difference, with the experimental ones re-sampled on the numerical mesh using the previously discussed moving least squares (MLS) procedure. The same domain mapping algorithm is used to exchange motion and loads at the nodes between MBDyn and the fluid solver implemented in FEniCS during the coupled fluid-structure solution when the interface nodes of the structure and fluid domains do not match. The structural grid, implemented within the multibody simulation environment provided by MBDyn, consists of 8×16 four-node membrane elements, involving 153 structural nodes (and 153 rigid body elements when

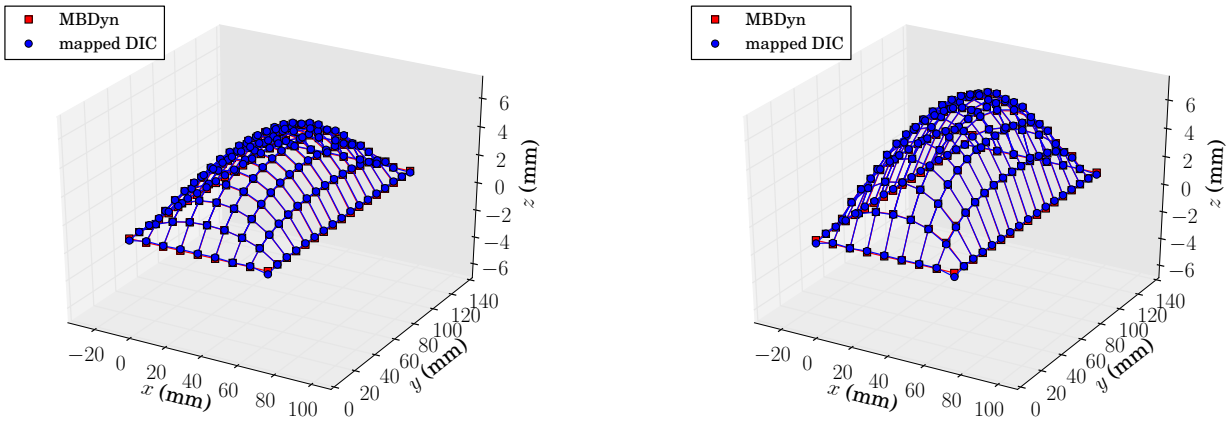

(a) 300 Pa.

(b) 500 Pa.

Figure 6. Numerical/experimental correlation of hydrostatic pressure problem.

a dynamic model needs to be used). Although not involved in the presented test cases, the mass lumped in each node is computed from the latex rubber sheet portion associated with the node, which is uniformly distributed (see Table 2). The simulation volume was sized to be five times larger than the chord in the x-direction, two chord lengths above and below the wing (z-direction) and one to the side of the wing (y-direction). The volume was discretized into approximately 1 million tetrahedral volume cells, and 181k nodes. In this case, 20445 points were used to compute the fluid-structure interface matrix.

A comparison of the direct solution for smaller and larger values of the prestrain is performed to study how much the problem is dependent on the value of the prestrain [27, 33]. The membrane prestrain was introduced as accurately as possible at the nominal level, but could not be checked afterwards [29]. The fact that the numerical solutions with nominal prestrain present a very good correlation with the experiments, and that the solution is very sensitive to the amount of prestrain, suggest that the actual prestrain in the experiments was in accordance with the expected value. The inverse solution, instead, is insensitive to the amount of prestrain (matrix $\mathbf{T}$ of Eq. (10)) that is used to stabilize the solution process.

2. Inverse Survey

The deformed configuration of the previously investigated rectangular edge-clamped membrane is determined herein using the strain measurements derived from DIC, re-sampled (and smoothed) onto the numerical mesh using the previously discussed MLS procedure. The membrane dimensions, loading, boundary conditions, and material properties are the same as in the direct analysis case discussed above. A triangular mesh consisting of 8×16

elements has been used for the IFEM procedure.

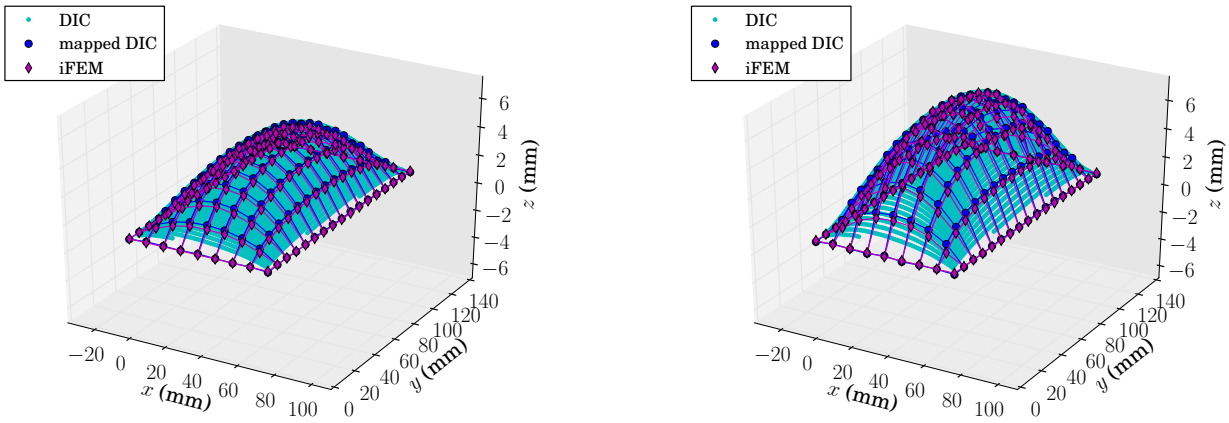

(a) 300 Pa. (b) 500 Pa.

Figure 7. IFEM/DIC correlation of hydrostatic pressure problem.

In Figs. 7(a) and 7(b) the deformation shape corresponding to the inverse FEM analysis for the problems with 300 Pa and 500 Pa of pressure difference are presented, along with the experimental data re-sampled on the numerical mesh, to validate the deformations predicted by the IFEM analysis.

The problem with 500 Pa of pressure difference appears to be essentially at convergence even with a mesh consisting of 8×16 elements [27], and the experimental displacements and those reconstructed using IFEM are in good agreement on the entire domain, including the maximum values.

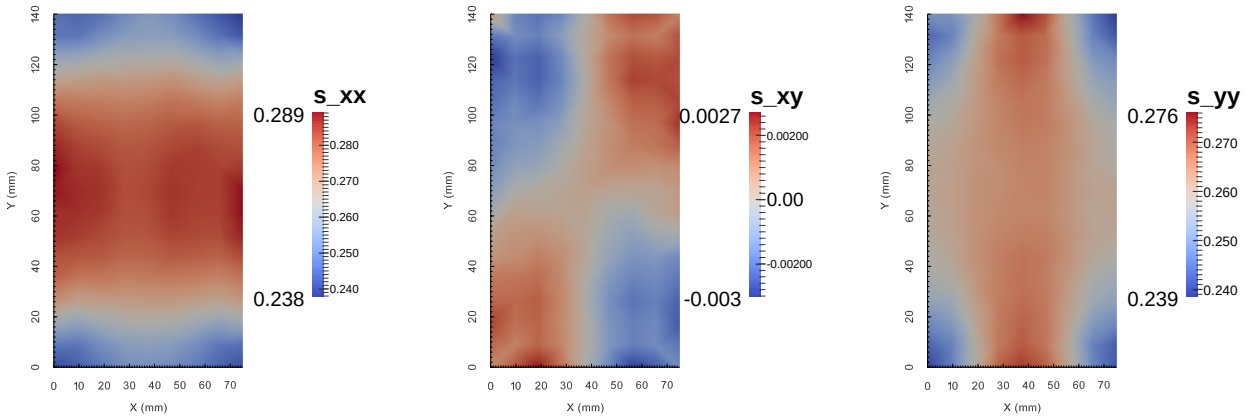

(a) σ_{xx} (MPa) (b) σ_{xy} (MPa) (c) σ_{yy} (MPa)

Figure 8. Membrane stress distribution (MPa) of a rectangular membrane subjected to 500 Pa of pressure difference.

The internal stresses for one particular hydrostatic pressure test at 500 Pa are shown in Fig. 8. The stress components σ_{xx} and σ_{yy} grow from the initial value, about 0.238 MPa, to a maximum value of the order of 0.289 MPa for σ_{xx} and 0.276 MPa for σ_{yy}, respectively, in the central portion of the membrane, where the extension is maximal. The cross term σ_{xy} remains negligible. Such a change, of the order of 20%, clearly shows that the approximation of constant membrane stress, which is at the roots of the linearized membrane model, is not applicable to problems of this type.

Consider for example a linearized model of a rectangular membrane, with $x \in [0, a]$, $y \in [0, b]$, prestressed by $\sigma_x^0 = \sigma_y^0 = \sigma^0$, $\tau_{xy}^0 = 0$, simply supported at all sides, which is governed by the partial differential equation

$$h\sigma^0 \left(w_{/xx} + w_{/yy} \right) = \Delta p \tag{14}$$

Approximating the transverse displacement with

$$w(x, y) = \sum_{i,j} \sin\left(i\pi \frac{x}{a} \right) \sin\left(j\pi \frac{y}{b} \right) \, q_{ij} \tag{15}$$

which complies with the boundary conditions, the solution is

$$q_{ij} = \frac{1}{\left(\frac{\pi}{2}\right)^4 ij \left(i^2 \frac{b}{a} + j^2 \frac{a}{b} \right)} \frac{ab}{h\sigma^0} \Delta p \tag{16}$$

For $\Delta p = 500$ Pa, the approximate solution (15) quickly converges (e.g., for $i = j = 5$) to a maximum displacement value, 9.34 mm, which is about 27% larger than the solution of the corresponding nonlinear problem, 7.35 mm, as shown in Fig. 9. Fig. 9 represents the

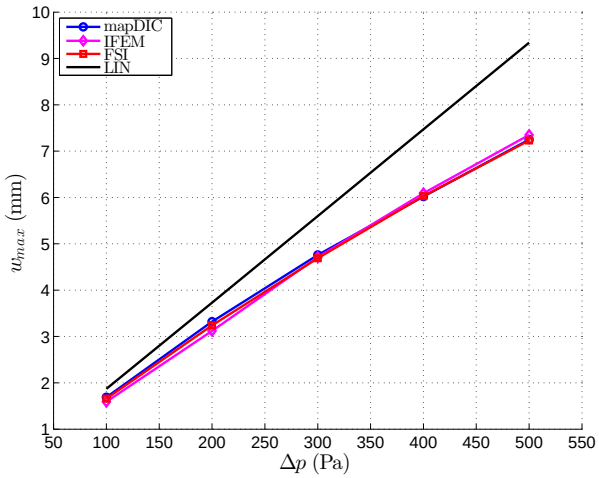

Figure 9. Hydrostatic pressure test: maximum transverse displacement as a function of hydrostatic pressure.

maximum mapped (labeled "EXP") and predicted (labeled "IFEM" and "FSI", respectively) camber, as a function of the applied hydrostatic pressure, together with the maximum displacement value obtained computing the solution with a linearized model (labeled "LIN"), as discussed above. As we can easily see, a linearized structural model is inadequate for the problem at hand.

The pressure distribution for one particular hydrostatic pressure test at 300 Pa is shown in Fig. 10, in order to compare a known input data, in this case a static pressure, with the estimated load. In fact, with a known input to the system, the output from the loads estimation procedure could be directly evaluated for its accuracy. The Figure on the left shows the ideal hydrostatic pressure applied to the membrane. The center Figure shows the pressure distribution calculated directly from DIC displacement measurements remapped onto the numerical mesh grid as required by the IFEM procedure. The Figure on the right shows the estimated pressure distribution from the displacements reconstructed by IFEM analysis. The results from the hydrostatic pressure test show favorable results [41]: the average

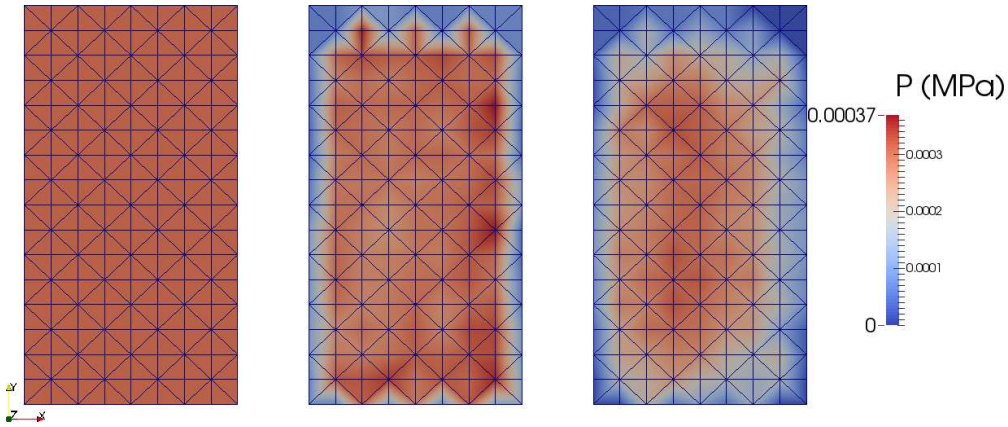

Figure 10. Pressure distribution (MPa) of a rectangular membrane subjected to 300 Pa of pressure difference (left: ideal pressure distribution; center: re-mapped DIC pressure distribution; right: IFEM pressure distribution).

hydrostatic pressure estimates are reasonably close to the actual applied hydrostatic load, and the error between the resultant (normal) force from the estimated pressure distributions and the one from the ideal hydrostatic pressure distribution is relatively small, as shown in Table 3.

Table 3. Resultant normal force error (not considering the near-boundary region) with respect to the nominal value.

Re-mapped DIC displacements	0.42	%
Inverse FEM analysis displacements	8.1	%

C. Wind Tunnel Tests

In the second scenario, a membrane wing was placed in a low speed wind tunnel, and wind speed and angle of attack were varied. Aerodynamic loads generated by the wing were measured, and DIC measurements of the membrane deformation were taken.

The experiments conducted at OSU also involved wind tunnel tests of various 2:1 aspect ratio, rectangular, perimeter reinforced membrane wings. The membrane dimensions and the material properties are same as in Section B, see Table 2. The wing was constructed of a steel frame, sandwiching a pre-tensioned rubber latex membrane. The overall geometry was 140 mm $\times$ 75 mm, with a frame width and thickness of 5 mm and 1 mm respectively. All

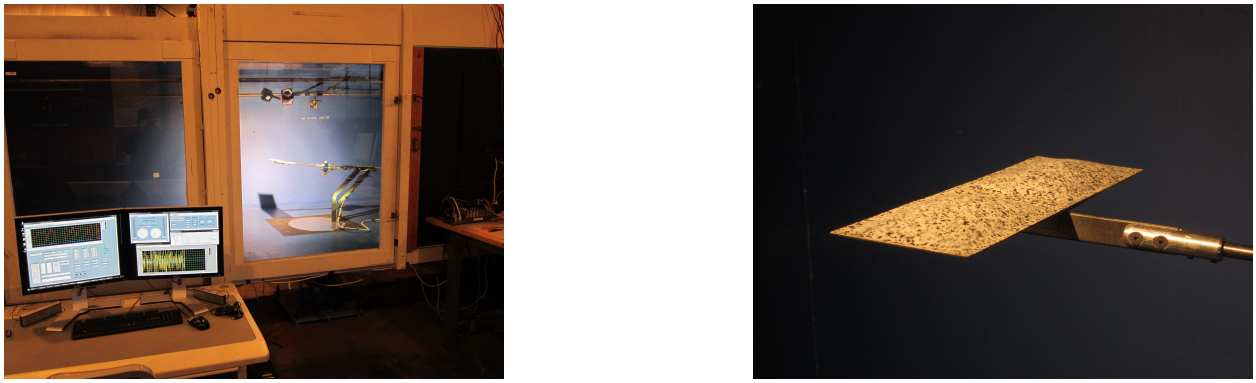

(a) Overall. (b) Zoom.

Figure 11. Wind Tunnel Apparatus.

experiments were conducted in a low-speed wind tunnel located at Oregon State University, Corvallis (OR). It is shown in Figs. 11(a) and 11(b). The wind tunnel had a closed loop, closed test section, capable of speeds from 1 to 18 meters per second (m/s) and with a 1.3 $\times$ 1.5 m test section.

Wind tunnel tests were performed for three flight speeds (12, 15 and 18 m/s) that are typical for MAV operation, at three pre-stall angles of attack (3, 6 and 9 deg), with three prestrain values (2, 3.5 and 5%). The maximum Reynolds number is 67000. At each flight condition, the aerodynamic loads are measured with a six component sting balance. At the same time, the undeformed wing shape and the strain field are measured using DIC. To evaluate the validity of the purposed approach, experimental wind tunnel loads and DIC displacements are compared to those obtained with the purposed model under varying conditions of flow velocity, AoA and initial prestrain.

1. Direct Survey

Figures 13(a) and 13(b) compare the numerical results, with the experimental ones re-sampled on the numerical mesh grid using the MLS procedure. The same domain mapping

algorithm is adopted to exchange motion and loads at the nodes between MBDyn and the fluid solver implemented in FEniCS during the coupled fluid-structure solution.

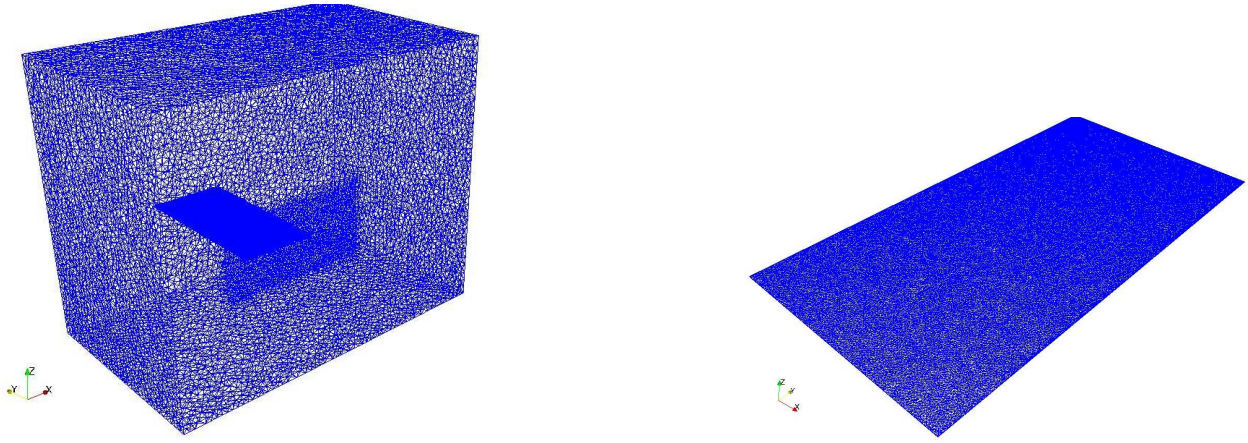

(a) Half span CFD simulation domain.

(b) Meshed membrane wing.

Figure 12. CFD domain.

The structural grid is identical to the one used for the hydrostatic pressure tests (see Section B). It consists of 8×16 four-node membrane elements, involving 153 structural nodes, and thus 153 rigid body elements. Moreover, to model the steel frame surrounding the membrane wing, 24 "three-nodes" beams were added to the structural model (their aerodynamic contribution was neglected). Thus, in the current case, the mass lumped in each node is computed from the latex rubber sheet portion associated with the node, which is uniformly distributed, and, for the boundary nodes, from the portion of the steel frame associated with the node (see Table 2). A symmetric boundary condition was applied at the centerline of the wing in order to reduce computational time. The half span simulation volume consists of approximately 324k nodes and 2 millions tetrahedrons. The computational domain corresponds to half of the dimensions of the wind tunnel test camera used for the experiments (see Fig. 11(a)). In the current case, 49729 points were used to compute the fluid-structure interface matrix. The simulation volume is shown in Figs. 12(a) and 12(b).

2. Inverse Survey

The deformed configuration of the previously investigated rectangular membrane is determined herein using the strain measurements derived from DIC, re-sampled onto the numerical mesh using the previously discussed MLS procedure. The membrane dimensions, loading, boundary conditions, and material properties are the same as in the direct analysis case discussed above, see Table 2. A triangular mesh consisting of 8×16 elements has been used for the IFEM procedure: the strain measurements from DIC are re-mapped (and smoothed out) onto this virtual strain measurement grid, and used as inputs for the IFEM analysis.

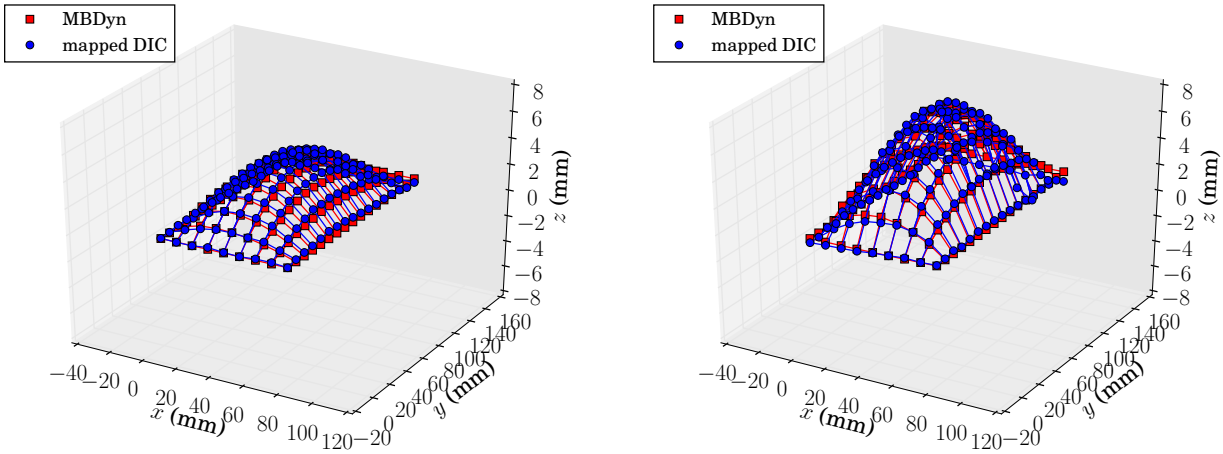

(a) V = 12 m/s, AoA = 3 deg, PS = 2%. (b) V = 18 m/s, AoA = 6 deg, PS = 5%.

Figure 13. DIC/MBDyn correlation of wind tunnel tests.

Figures 14(a) and 14(b) compare the deformation shape corresponding to the inverse FEM analysis with the experimental data re-sampled on the numerical mesh.

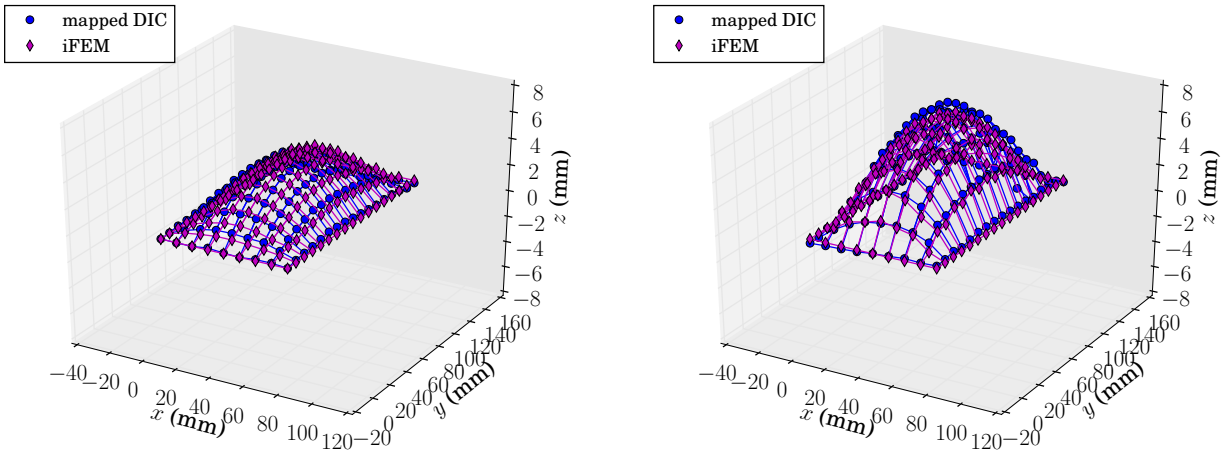

(a) V = 12 m/s, AoA = 3 deg, PS = 2%. (b) V = 18 m/s, AoA = 6 deg, PS = 5%.

Figure 14. IFEM/DIC correlation of wind tunnel tests.

3. Static Model

Utilizing DIC data, the prediction of max camber, $\frac{z(\alpha)}{c}$, where c is the chord, can be evaluated for its accuracy and overall physical behavior.

Figures 15(a) and 15(b) represent the average max (mapped) measured (labeled "EXP")

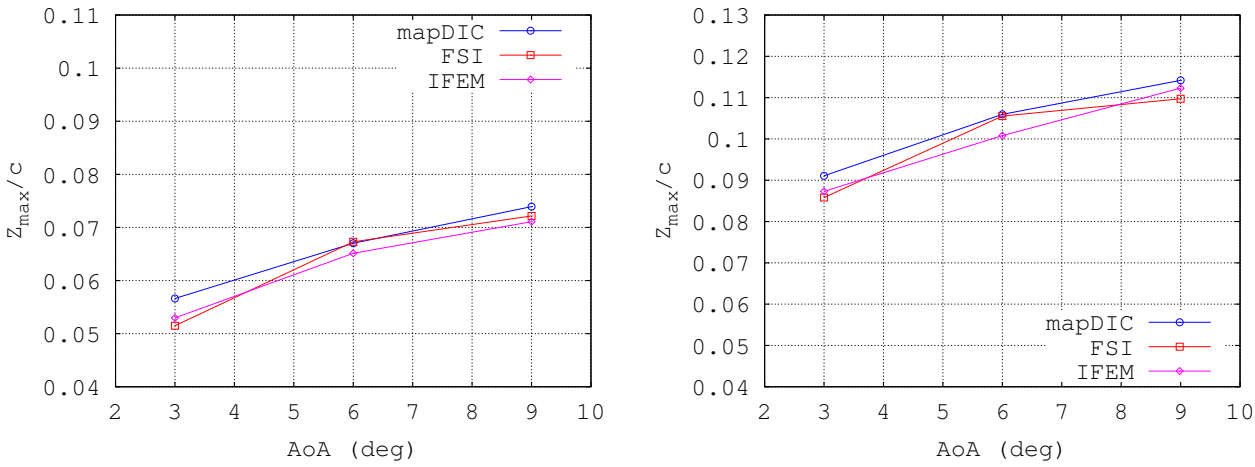

(a) V = 12 m/s, PS = 2%. (b) V = 18 m/s, PS = 5%.

Figure 15. Measured max displacement from DIC data and predicted max displacement.

and predicted (labeled "FSI" and "IFEM") static camber for two different values of prestrain, 2% and 5%, respectively, and for a flow velocity of $V = 12$ and 18 m/s. As expected, the measured and predicted displacement are primarily characterized by an adaptive inflation, which increases the local camber.

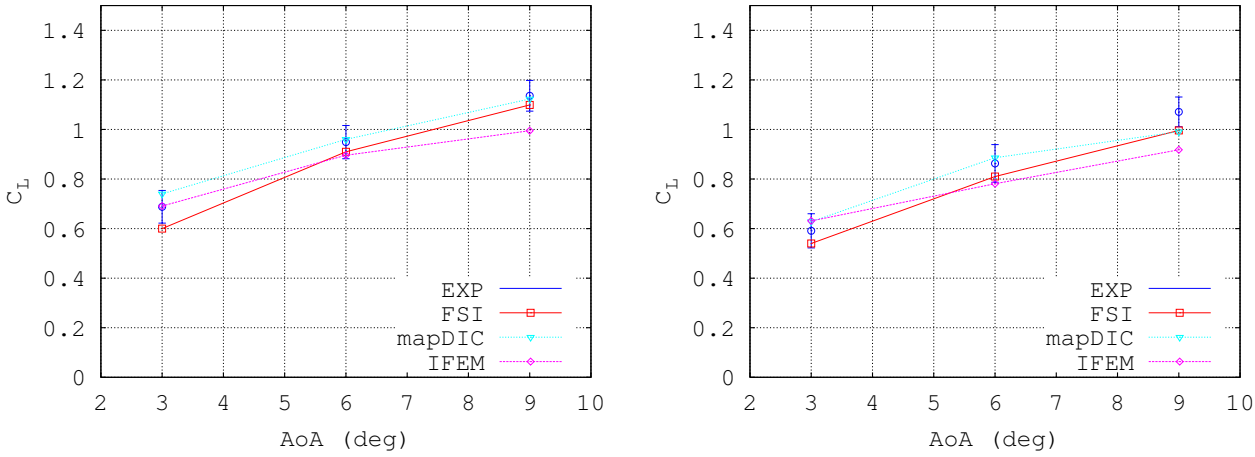

(a) V = 12 m/s, PS = 2%. (b) V = 18 m/s, PS = 5%.

Figure 16. Static lift model and wind tunnel data.

Figures 16(a) and 16(b) show the lift coefficient measured by the load cell attached to the wing (labeled "EXP"). They show the lift coefficient calculated by the coupled fluid-structure simulation (labeled "FSI"), and also the estimated lift coefficients found by integrating the estimated pressure distributions (calculated from the remapped full-field DIC measurements, labeled "mapDIC", and from the estimated displacements via inverse anal-

ysis, labeled "IFEM", respectively) to find the normal load, converting it into lift via the AoA, and finally calculating the lift coefficient.

It is worth noticing that those curves are nearly invariant with respect to changes in flow velocity within the range of this study (Re = 45k–67k). The error bars in the previous figures represent the standard deviations, $\sigma_{C_L^{\text{exp}}}$, which are presented for reference in Table 4.

VI. Conclusions

This work presents the direct and inverse analysis of membrane elements for fluid-structure interaction problems. A membrane inverse analysis based on a three-node membrane element was developed based on a least squares smoothing functional that employs the complete set of strain measures. A four-node membrane element was implemented in a multibody-based co-simulation analysis for the direct simulation of coupled fluid-structure problems. The inverse analysis has been verified by reconstructing the deformed solution obtained with the analogous direct formulation applied on a different mesh and subsequently re-sampled; both the direct and the inverse analyses have been validated by comparing the direct prediction and the reconstructed deformation with experimental data for prestressed rectangular membranes subjected to hydrostatic pressure loads. Finally, an approach to estimating aerodynamic load present on a flexible membrane wing from elastic strain sensor was developed. The proposed analysis enables accurate and computationally efficient high-fidelity deformation reconstruction solutions. It is therefore applicable to both static and dynamic problems. Hydrostatic pressure tests were considered in order to compare a known input load to the estimated load. Results were favorable: the average hydrostatic pressure estimate was reasonably close to the actual applied hydrostatic pressure. In addition, the error introduced in the estimated pressure distribution can be seen in the irregularity of the estimated pressure distribution compared to the ideal pressure distribution. The proposed procedure for the reconstruction of shape and distributed loads is able to operate at sample rates of the order of 30 Hz, thus meeting the initial real-time operation requirement.

Acknowledgments

Effort sponsored by the Air Force Office of Scientific Research, Air Force Material Command, USAF, under grant number FA8655-12-1-2114, technical monitor Dr. Gregg Abate. The U.S. Government is authorized to reproduce and distribute reprints for Governmental purpose notwithstanding any copyright notation thereon.

Table 4. Wind tunnel test results.

V(m/s)	AoA(deg)	PS (%)	$C_L^{(\mathrm{exp})}$	$\sigma_{C_L^{(\mathrm{exp})}}$	$C_L^{(\mathrm{fsi})}$	$C_{Lp^{(\mathrm{m})}}$	$C_{Lp^{(\mathrm{ifem})}}$	$w^{(\mathrm{m})}$ (mm)	$w^{(\mathrm{fsi})}$ (mm)	$\mathrm{Err}_{w^{(\mathrm{fsi})}}$ (%)	$w^{(\mathrm{ifem})}$ (mm)	$\mathrm{Err}_{w^{(\mathrm{ifem})}}$ (%)
12	3	2	0.688	0.066	0.600	0.740	0.691	4.19	3.81	9.07	3.92	6.44
12	6	2	0.949	0.067	0.910	0.960	0.896	4.96	4.98	0.40	4.82	2.82
12	9	2	1.136	0.062	1.099	1.123	0.995	5.47	5.34	2.38	5.26	3.84
15	3	2	0.688	0.066	0.666	0.718	0.721	6.57	6.63	0.91	6.58	0.15
15	6	2	0.949	0.067	0.985	1.008	0.978	7.32	7.18	1.91	7.17	2.05
15	9	2	1.136	0.062	1.111	1.163	1.121	7.69	7.52	2.21	7.53	2.08
15	3	5	0.591	0.069	0.500	0.554	0.594	4.15	3.77	9.16	3.97	4.34
15	6	5	0.863	0.076	0.820	0.816	0.801	5.16	5.07	1.74	4.95	4.07
15	9	5	1.071	0.060	0.990	0.928	0.967	5.84	5.77	1.20	5.80	0.68
18	3	5	0.591	0.069	0.540	0.628	0.631	6.74	6.35	5.79	6.46	4.15
18	6	5	0.863	0.076	0.810	0.886	0.781	7.84	7.81	0.38	7.46	4.85
18	9	5	1.071	0.060	0.996	0.991	0.918	8.45	8.12	3.91	8.31	1.66

References

[1] Sutton, M. A., Turner, J. L., Bruck, H. A., and Chae, T. A., "Full-field representation of discretely sampled surface deformation for displacement and strain analysis," *Experimental Mechanics*, Vol. 31, No. 2, 1991, pp. 168–177, doi:10.1007/BF02327571.

[2] Waldman, R. M., Song, A. J., Riskin, D. K., Swartz, S. M., and Breuer, K. S., "Aerodynamic behavior of compliant membranes as related to bat flight," *38th AIAA Fluid Dynamics Conference and Exhibit Seattle, Washington, USA*, 2008.

[3] Kamakoti, R. and Shyy, W., "Fluid-structure interaction for aeroelastic applications," *Progress in Aerospace Sciences*, Vol. 40, No. 8, November 2004, pp. 535–558, 10.1016/j.paerosci.2005.01.001.

[4] Shyy, W., Ifju, P., and Viieru, D., "Membrane Wing-Based Micro Air Vehicles," *Applied Mechanics Reviews*, Vol. 58, No. 4, July 2005, pp. 283–301, doi:10.1115/1.1946067.

[5] Gordnier, R. E., Chimakurthi, S. K., Cesnik, C. E. S., and Attar, P. J., "High-Fidelity Aeroelastic Computations of a Flapping Wing with Spanwise Flexibility," *49th AIAA Aerospace Sciences Meeting*, Orlando, Florida, USA, January 4–7 2011, AIAA-2011-570.

[6] Aono, H., Chimakurthi, S. K., Wu, P., Sällström, E., Stanford, B. K., Cesnik, C. E. S., Ifju, P., Ukeiley, L., and Shyy, W., "A Computational and Experimental Study of Flexible Flapping Wing Aerodynamics," *48th AIAA Aerospace Sciences Meeting*, Orlando, Florida, January 4–7 2010, AIAA-2010-554.

[7] Ho, S., Nassef, H., Pornsinsirirak, N., Tai, Y.-C., and Ho, C.-M., "Unsteady aerodynamics and flow control for flapping wing flyers," *Progress in Aerospace Sciences*, Vol. 39, No. 8, 2003, pp. 635–681.

[8] Suryadi, A. and Obi, S., "The estimation of pressure on the surface of a flapping rigid plate by stereo PIV," *Experiments in fluids*, Vol. 51, No. 5, 2011, pp. 1403–1416.

[9] Heathcote, S., Wang, Z., and Gursul, I., "Effect of spanwise flexibility on flapping wing propulsion," *Journal of Fluids and Structures*, Vol. 24, No. 2, February 2008, pp. 183–199, doi:10.1016/j.jfluidstructs.2007.08.003.

[10] Heathcote, S., Martin, D., and Gursul, I., "Flexible Flapping Airfoil Propulsion at Zero Freestream Velocity," *AIAA Journal*, Vol. 42, No. 11, November 2004, pp. 2196–2204, doi:10.2514/1.5299.

[11] Shyy, W., Berg, M., and Ljungqvist, D., "Flapping and flexible wings for biological and micro air vehicles," *Progress in Aerospace Sciences*, Vol. 35, No. 5, 1999, pp. 455–505.

[12] Stanford, B., Albertani, R., and Ifju, P., "Inverse Methods to Determine the Aerodynamic Forces on a Membrane Wing," *48th AIAA/ASME/ASCE/AHS/ASC Structures, Structural Dynamics, and Materials Conference*, Honolulu, Hawaii, April 23–26 2007, AIAA 2007-1984.

[13] Gopalakrishnan, P. and Tafti, D. K., "Effect of Wing Flexibility on Lift and Thrust Production in Flapping Flight," *AIAA Journal*, Vol. 48, No. 5, May 2010, pp. 865–877, doi:10.2514/1.39957.

[14] Stanford, B., Sytsma, M., Albertani, R., Viieru, D., Shyy, W., and Ifju, P., "Static aeroelastic model validation of membrane micro air vehicle wings," *AIAA journal*, Vol. 45, No. 12, 2007, pp. 2828–2837.

[15] Lian, Y. and Shyy, W., "Laminar-turbulent transition of a low Reynolds number rigid or flexible airfoil," *AIAA journal*, Vol. 45, No. 7, 2007, pp. 1501–1513.

[16] Foster, N. F. and Dulikravich, G. S., "Three-dimensional aerodynamic shape optimization using genetic and gradient search algorithms," *Journal of Spacecraft and Rockets*, Vol. 34, No. 1, 1997, pp. 36–42.

[17] Tessler, A. and Spangler, J. L., "A least-squares variational method for full-field reconstruction of elastic deformations in shear-deformable plates and shells," *Comput. Meth. Appl. Mech. Engng.*, Vol. 194, No. 2–5, 2005, pp. 327–339, doi:10.1016/j.cma.2004.03.015.

[18] Shkarayev, S., Krashantisa, R., and Tessler, A., "An Inverse Interpolation Method Utilizing In-Flight Strain Measurements for Determining Loads and Structural Response of Aerospace Vehicles," *Proceedings of Third International Workshop on Structural Health Monitoring*, 2001, pp. 336–343.

[19] Kyriacou, S. K., Shah, A. D., and Humphrey, J. D., "Inverse Finite Element Characterization of Nonlinear Hyperelastic Membranes," *Journal of Applied Mechanics*, Vol. 64, No. 2, 1997, pp. 257–262, doi:10.1115/1.2787301.

[20] Kroon, M., "An Efficient Method for Material Characterisation of Hyperelastic Anisotropic Inhomogeneous Membranes Based on Inverse Finite-Element Analysis and an Element Partition Strategy," *The Quarterly Journal of Mechanics and Applied Mathematics*, Vol. 63, No. 2, 2010, pp. 201–225, doi:10.1093/qjmam/hbq004.

[21] Aernouts, J., Couckuyt, I., Crombecq, K., and Dirckx, J. J. J., "Elastic characterization of membranes with a complex shape using point indentation measurements and inverse modelling," *International Journal of Engineering Science*, Vol. 48, No. 6, 2010, pp. 599–611, doi:10.1016/j.ijengsci.2010.02.001.

[22] Masarati, P., Morandini, M., and Solcia, T., "A Membrane Element for Micro-Aerial Vehicle Fluid-Structure Interaction," *2nd Joint International Conference on Multibody System Dynamics*, edited by P. Eberhard and P. Ziegler, Stuttgart, Germany, May 29–June 1 2012.

[23] Alioli, M., *Coupled Fluid-Structure Simulation of Flapping Wings*, Master's thesis, Politecnico di Milano, 2011.

[24] Alioli, M., Morandini, M., and Masarati, P., "Coupled Multibody-Fluid Dynamics Simulation of Flapping Wings," *ASME IDETC/CIE*, Portland, OR, August 4–7 2013, DETC2013-12198.

[25] Alioli, M., Morandini, M., Masarati, P., Ghiringhelli, G. L., Carpenter, T., and Albertani, R., "Nonlinear Membrane Inverse Finite Elements," *ICNAAM*, Rhodes, GR, September 22–28 2014.

[26] Logg, A., Mardal, K.-A., and Wells, G., editors, *Automated Solution of Differential Equations by the Finite Element Method*, Vol. 84 of *Lecture Notes in Computational Science and Engineering*, Springer Berlin Heidelberg, Berlin, Heidelberg, 2012.

[27] Alioli, M., Morandini, M., Masarati, P., Carpenter, T., and Albertani, R., "Nonlinear Membrane Direct and Inverse FEM Analysis," *ASME IDETC/CIE*, Buffalo, NY, August 17–20 2014, DETC2014-34476.

[28] Bakushinsky, A. and Goncharsky, A., *Ill-posed problems: theory and applications*, Kluwer Academic Publisher, Dordrecht, Boston, London, 1994.

[29] Carpenter, T. J. and Albertani, R., "Aerodynamic Load Estimation: Pressure Distribution from Virtual Strain Sensors for a Pliant Membrane Wing," *54th AIAA/ASME/ASCE/AHS/ASC Structures, Structural Dynamics, and Materials Conference*, April 8-11 2013, doi:10.2514/6.2013-1917.

[30] Quaranta, G., Masarati, P., and Mantegazza, P., "A Conservative Mesh-Free Approach for Fluid Structure Interface Problems," *Coupled Problems 2005*, Santorini, Greece, May 24–27 2005.

[31] Levenberg, K., "A Method for the Solution of Certain Non-Linear Problems in Least Squares," *Quarterly of Applied Mathematics*, Vol. 2, 1944, pp. 164–168.

[32] Marquardt, D., "An Algorithm for Least-Squares Estimation of Nonlinear Parameters," *Journal of the Society for Industrial and Applied Mathematics*, Vol. 11, No. 2, 1963, pp. 431–441, doi:10.1137/0111030.

[33] Alioli, M., Morandini, M., Masarati, P., Carpenter, T., and Albertani, R., "Nonlinear Membrane Inverse Finite Element Model For Pliant Wings," *SCITECH*, Kissimmee, FL, January 5–9 2015, AIAA2015-2051.

[34] Do Carmo, M. P., *Differential geometry of curves and surfaces*, Prentice-Hall, Englewood Cliffs, 1976.

[35] Ciarlet, P. G. and Larsonneur, F., "On the recovery of a surface with prescribed first and second fundamental forms," *Journal des Mathematiques Pures et Appliquees*, Vol. 81, 2002, pp. 167–185.

[36] Chapelle, D. and Bathe, K.-J., *The finite element analysis of shells – fundamentals*, Springer, 2nd ed., 2011.

[37] Masarati, P., Morandini, M., and Mantegazza, P., "An efficient formulation for general-purpose multibody/multiphysics analysis," *J. of Computational and Nonlinear Dynamics*, Vol. 9, No. 4, 2014, pp. 041001, doi:10.1115/1.4025628.

[38] Hoffman, J. and Johnson, C., *Computational Turbulent Incompressible Flow*, Vol. 4 of *Applied Mathematics: Body and Soul*, Springer, 2007, doi:10.1007/978-3-540-46533-1.

[39] Simo, J. C. and Rifai, M. S., "A class of mixed assumed strain methods and the method of incompatible modes," *Intl. J. Num. Meth. Engng.*, Vol. 29, No. 8, 1990, pp. 1595–1638, doi:10.1002/nme.1620290802.

[40] Andelfinger, U. and Ramm, E., "EAS-elements for two-dimensional, three-dimensional, plate and shell structures and their equivalence to HR-elements," *Intl. J. Num. Meth. Engng.*, Vol. 36, No. 8, 1993, pp. 1311–1337, doi:10.1002/nme.1620360805.

[41] Alioli, M., Morandini, M., Masarati, P., Carpenter, T., Albertani, R., and Osterberg, N. B., "Membrane Shape and Transverse Load Reconstruction Using Inverse FEM," *ASME IDETC/CIE*, Boston, MA, August 2–5 2015, DETC2015-46753.